Dirac semimetal phase in hexagonal LiZnBi

Wendong Cao,[1,2] Peizhe Tang,[3] Yong Xu,[1,2,4] Jian Wu,[1,2] Bing-Lin Gu,[2,5] and Wenhui Duan[1,2,5,*]

[1]*Department of Physics and State Key Laboratory of Low-Dimensional Quantum Physics, Tsinghua University, Beijing 100084, China*

[2]*Collaborative Innovation Center of Quantum Matter, Tsinghua University, Beijing 100084, China*

[3]*Department of Physics, McCullough Building, Stanford University, Stanford, California 94305-4045, USA*

[4]*RIKEN Center for Emergent Matter Science (CEMS), Wako, Saitama 351-0198, Japan*

[5]*Institute for Advanced Study, Tsinghua University, Beijing 100084, China*

(Received 3 July 2017; published 11 September 2017)

Based on first-principles calculations, we find that LiZnBi, a metallic hexagonal ABC compound, has a pair of three-dimensional Dirac nodes and exhibits nontrivial topological properties under proper strain configurations. The nontrivial topological nature of the strained LiZnBi is directly demonstrated by calculating its $\mathbb{Z}_2$ index and the surface states. The low-energy states are shown to be sensitive to strain configurations, and we propose that these nontrivial topological properties can be observed under compressive in-plane strain in experiments. The finding of the Dirac semimetal phase in LiZnBi may intrigue further research on the topological properties of hexagonal ABC materials and promote new practical applications.

DOI: 10.1103/PhysRevB.96.115203

I. INTRODUCTION

Recently, topologically nontrivial quantum materials with gapless band dispersions including Dirac semimetals and Weyl semimetals began to attract increasing attention [1] due to the existence of Fermi arcs on surfaces [2–6] and anomalous transport phenomena [7–10]. A Weyl semimetal has multiple crossings with nontrivial Berry fluxes near the Fermi level, in which either spatial inversion symmetry (TaAs class [11,12]) or time-reversal symmetry (pyrochlore iridates [2]) is broken. The Dirac fermions can be regarded as two copies of Weyl fermions in Dirac semimetals, which are protected by crystal symmetry regardless of time-reversal symmetry. The crystal symmetry can be symmorphic (such as Na_3Bi [4,13] and Cd_3As_2 [14,15]) or nonsymmorphic (such as β-cristobalite BiO_2 [16] and antiferromagnetic CuMnAs [17]). The Dirac or Weyl fermions in these materials mimic their counterparts in high-energy physics: the dispersions near the Dirac or Weyl node are linear along all three directions and the Lorentz invariance is respected. Very recently, it has also been shown that there exist type-II Dirac and Weyl semimetals in condensed matter [18,19], where the Dirac cones are strongly titled and the Lorentz invariance is violated. In experiments, the type-II Dirac and Weyl semimetals can be realized in the $PtSe_2$ class [20,21] and WTe_2 [22], $MoTe_2$ [23], respectively.

From the view of material science, ABC compounds represent an interesting compound family with many exotic properties. Recent theoretical calculations indicated that the hexagonal ABC compounds in the LiGaGe structure can be a new family of ferroelectric and piezoelectric materials [24]. Their crystal structure is relatively simple and some of them have polarizations with switching barriers comparable to those of $BaTiO_3$. Further studies showed that KMgBi, one member of this family, is also a three-dimensional strong topological insulator [25]. The interplay between ferroelectricity and nontrivial topology can induce unique properties of the topological surface states [25,26]. Different from topological insulators, a topological semimetal cannot be ferroelectric or piezoelectric due to its gapless bulk spectrum. But when a topological semimetal shares the same polar structure with its piezoelectric substrate, the piezoelectric effect can provide an effective approach to tuning its lattice structure and electronic properties. Therefore, the hexagonal ABC compounds can be a promising class of topological semimetals for their potential versatility.

In this work, based on first-principles calculations, we show that unstrained hexagonal LiZnBi hosts a pair of Dirac points; but the corresponding Fermi arc surface states strongly couple with the projections of bulk states around the Γ point, and thus can hardly be observed in experiments. Via applying strain without breaking crystal symmetry, the hexagonal LiZnBi becomes an ideal three-dimensional (3D) Dirac semimetal. By analyzing the orbital character of low-energy states, we find that nontrivial topological characters of strained LiZnBi result from a band inversion at the Γ point, and its topological index and nontrivial Fermi arc surface states are confirmed by our calculations. Finally, we study the response of low-energy states to different strain configurations and find out that the topological features of the Dirac nodes can be experimentally revealed in LiZnBi by applying in-plane compressive strain.

II. METHODS

The first-principles calculations are carried out by using density functional theory (DFT) with the projector augmented wave method [27,28], as implemented in the Vienna *ab initio* simulation package, VASP [29]. A plane-wave basis set is used with a kinetic-energy cutoff of 300 eV. With $10 \times 10 \times 6$ Monkhorst-Pack k points and the local-density approximation (LDA) [30,31] for the exchange-correlation interactions between electrons, the atomic structure is fully relaxed until the residual forces are less than 1×10^{-3} eV/Å. Then we used the modified Becke-Johnson exchange potential [32,33] together with LDA for the correlation potential to get the accurate electronic structure, where the spin-orbit coupling is also included. The maximally localized Wannier functions are obtained by the program WANNIER90 [34]. The Green's

*dwh@phys.tsinghua.edu.cn

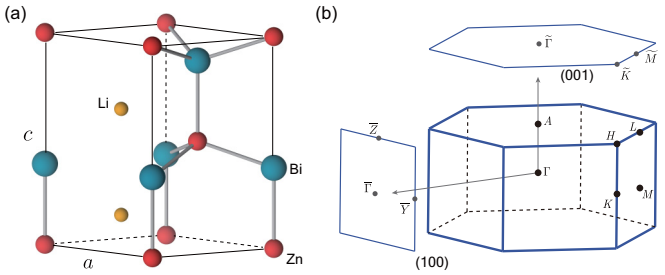

FIG. 1. (a) Lattice structure of LiZnBi with the space group $P6_3mc$, where a and c are two lattice constants. Zn and Bi atoms at Wyckoff positions $2b$ form a wurtzite structure, while Li atoms are located at $2a$. (b) The first Brillouin zone and its projections on (100) and (001) surfaces. High-symmetry points are labeled.

function method [35] is used to calculate the surface electronic spectrum and surface states.

III. RESULTS AND DISCUSSION

The stable lattice structure of LiZnBi, shown in Fig. 1(a), belongs to the space group $P6_3mc$. Li^+ ions occupy the interstitial sites of the wurtzite lattice of $ZnBi^-$ [36]. The calculated equilibrium lattice constants of the wurtzite structure are $a_0 = 4.47$ Å and $c_0 = 7.28$ Å, close to those experimental values ($a_0 = 4.58$ Å and $c_0 = 7.38$ Å) reported in the Inorganic Crystal Structural Database [37]. The first Brillouin zones of the bulk, (001) surface, and (100) surface are shown in Fig. 1(b).

Figure 2 shows the calculated band structures of LiZnBi without and with strain. In both cases, the spin-orbit coupling (SOC) is fully considered. We can see that the low-energy states are mainly located near the Γ point. For the unstrained case, some states along the M-L line also contribute to the 3D Fermi surface. Interestingly, even though the inversion symmetry is broken in the lattice structure, all the bands along the A-Γ line are doubly degenerate. Note that the little group is C_{6v} for any k point along that line. The double degeneracy is protected by the combination of C_6 rotation symmetry and mirror symmetry because these two symmetry operators do not commute with each other. For the states at the Γ point (labeled by their representations in Fig. 2), our calculations indicate that the $\Gamma_7(s)$ and Γ_8 states are dominated by s orbitals of Zn and Bi atoms and the Γ_8 states also have a substantial component of Bi-p_z orbitals. In contrast, the Γ_9 and $\Gamma_7(p)$ states are mainly contributed by $p_x \pm ip_y$ orbitals and p_z orbitals of Bi atoms, respectively. Since the states at k points along the A-Γ line share the same little group with that at the Γ point, the representation labels for states at the Γ point also apply to four corresponding bands along the A-Γ line. As k moves from A to Γ, the main components of the Γ_9 and Γ_8 states change little because the coupling between states belonging to different representations is forbidden by crystal symmetry. For $\Gamma_7(p)$ and $\Gamma_7(s)$ states, the coupling mixes two states to change their main components very much. This effect can be clearly observed from the band structure along the A-Γ line in Fig. 2, where the size of the red dots represents the relative ratio of s orbitals from Zn and Bi atoms.

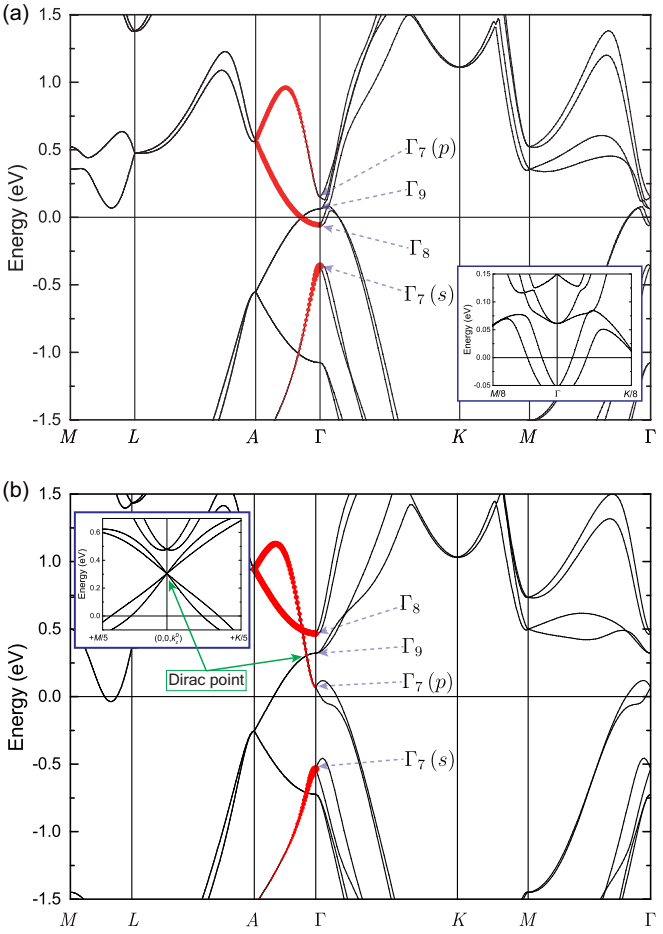

FIG. 2. Band structure along high-symmetry lines of LiZnBi in its (a) unstrained structure and (b) strained structure. For (b), $a = 0.98a_0$ and c is tuned to keep the volume of the unit cell. In both cases, spin-orbit coupling is included and the Fermi energy is set to zero. The size of the red dots along the A-Γ is proportional to the relative ratio of s orbitals from Zn and Bi atoms. At the Γ point, four low-energy states are labeled by their representations. The inset in (a) shows the band structure near the Γ point. In (b), the 3D Dirac point is pointed out by green arrows and the in-plane band dispersion around the Dirac point is shown in the inset.

For the unstrained case, the calculated band structure is shown in Fig. 2(a). At the Γ point, the band order is $\Gamma_7(p) > \Gamma_9 > \Gamma_8 > \Gamma_7(s)$. And for the states on these four energy levels. the $\hat{z}$ components of total angular momentum J_z are $\pm\frac{1}{2}$, $\pm\frac{3}{2}$, $\pm\frac{5}{2}$, and $\pm\frac{1}{2}$, respectively. In LiZnSb, that is a trivial semiconductor, $\Gamma_7(p)$ and Γ_9 belong to valence bands, while Γ_8 and $\Gamma_7(s)$ are conduction bands [38]. By substituting Sb atoms with Bi atoms, the chemical pressure in LiZnBi makes the p orbitals of Bi and Zn dominated around the Fermi level. In contrast to the trivial case, band inversions can be observed at the Γ point for this compound, in which both $\Gamma_7(s)$ and Γ_8 fall below $\Gamma_7(p)$ and Γ_9. And the strong coupling between $\Gamma_7(s)$ and $\Gamma_7(p)$ will push their corresponding bands away from the Fermi level. So only crossings between Γ_8 and Γ_9 states exist along the A-Γ line with nonzero $\mathbb{Z}_2$ charge. Considering different J_z for Γ_8 and Γ_9, we conclude that its $\mathbb{Z}_2$ charge is 1 [39–41]. However, due to Dirac nodes in LiZnBi

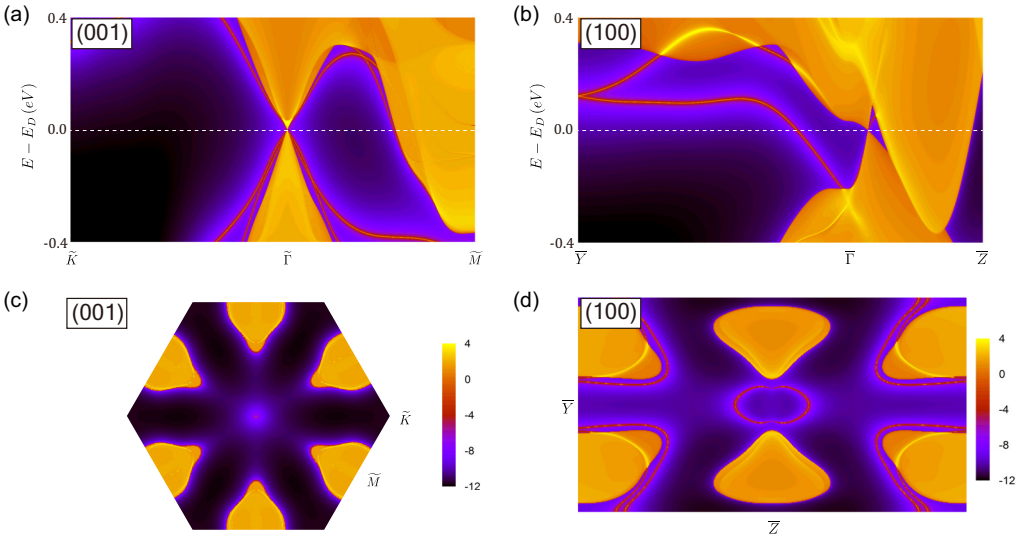

FIG. 3. LDOS for the (a),(c) (001) and (b),(d) (100) surface states of the strained LiZnBi. (a),(b) LDOS along high-symmetry lines where the energy level of the bulk Dirac points, E_D, is denoted by dashed white lines. (c),(d) The constant-energy contours at E_D.

burying inside bulk states, it is difficult to experimentally observe its topological properties, including Fermi arcs [5] and chiral anomaly [10] (see Appendix A). Therefore, the intrinsic LiZnBi is not a good Dirac semimetal candidate.

On the other hand, we find that the relative positions of four energy levels at the Γ point are sensitive to strain. This property provides an opportunity to tune electronic properties of LiZnBi by applying proper strain without breaking crystal symmetry. When the lattice constant c is enlarged and a is reduced, the band order changes, as shown in Fig. 2(b). Compared to the unstrained case in Fig. 2(a), the relative positions of the $\Gamma_7\,(p)$ and Γ_8 states are exchanged. Due to the symmetry-allowed coupling between $\Gamma_7\,(s)$ and $\Gamma_7\,(p)$, only band crossings between $\Gamma_7\,(p)$ and Γ_9 states are observed along the A-Γ line. These kinds of crossings are Dirac points with nonzero $\mathbb{Z}_2$ charge [42,43]. The detailed calculations for the $\mathbb{Z}_2$ index are shown in Appendix B. Herein, the crossing at $(0, 0, k_z^D \approx 0.074 \times 2\pi/c)$, indicated by green arrows in Fig. 2(b), can be described by the effective Hamiltonian near the Γ point (shown in Appendix C). The band dispersions are also linear along the in-plane momentum directions [see the inset of Fig. 2(b)], leading to a 3D Dirac cone. Time-reversal symmetry ensures that the same crossing also occurs at $(0, 0, -k_z^D)$. More importantly, a global gap at the Γ-K-M plane emerges, accompanied by the change of band order at the Γ point. So the Dirac nodes separate from the bulk bands around the Γ point in the momentum space, and LiZnBi in the strained structure becomes an ideal Dirac semimetal with a pair of Dirac points near the Fermi level.

To further confirm the topological nature of strained LiZnBi, we calculate its surface states on the (001) and (100) surfaces. Figure 3(a) shows the surface states on the (001) surface along $\widetilde{K}$-$\widetilde{\Gamma}$-$\widetilde{M}$. On this surface, two bulk Dirac points are projected onto the same $\widetilde{\Gamma}$ point. Their corresponding surface states are just one linear Dirac cone with band dispersion in the k_x-k_y plane. Figures 3(b) and 3(d) show the surface bands and Fermi surface contour at the Fermi level for the (100) surface. On this side surface, two bulk Dirac nodes related by time-reversal symmetry are projected to different points that are separated from the projected bulk states and connected by Fermi arcs. In projected surface bands, the nontrivial surface states terminate exactly at two projected Dirac points and merge into bulk states, which is a signature of nontrivial topology.

Because the strained LiZnBi is demonstrated to be a topological Dirac semimetal, it is necessary to understand how the strain affects the low-energy band structure and which type of strain mostly favors the existence of those topological properties. Our calculations indicate that main components of the low-energy states near the Γ point are s, p orbitals from Zn and Bi atoms. To simplify the following discussions, we focus on the wurtzite sublattice (Zn-Bi) instead of the whole LiGaGe structure. In conventional wurtzite materials, such as GaN and InN, both the spin-orbit coupling and the crystal-field splitting strongly affect the low-energy bands around the Fermi level [44]. Compared to spin-orbit coupling, the crystal-field splitting should be more sensitive to strain, especially anisotropic strain. Similar to the case in wurtzite materials, the crystal-field splitting here also originates from the lattice distortion, which breaks the tetrahedral symmetry (for one Zn/Bi atom, the length of the out-of-plane Zn-Bi bond is different from those of the other three bonds). For example, in the strained LiZnBi without SOC, the crystal-field effect removes the degeneracy between $p_{x,y}$ and p_z orbitals. And the crystal-field splitting Δ_{CF} is defined as the gap between $\Gamma_5(p_{x,y})$ and $\Gamma_1(p_z)$, as shown in Fig. 4(a). The dependence of Δ_{CF} on the two lattice constants (namely, a and c) is also calculated and the results are presented in Fig. 4(b). The crystal symmetry is preserved when the lattice constants differ from a_0 and c_0. It can be seen that Δ_{CF} is almost linearly proportional to $\frac{c}{a}$. And when $\Delta_{\mathrm{CF}} > 0.2$ eV, the variations of the lattice constants a and c have little effect on the crystal-field splitting Δ_{CF} as long as $\frac{c}{a}$ remains constant. The contour plot in Fig. 4(b) confirms an important role of the crystal-field splitting in opening the gap between $p_{x,y}$ and p_z orbitals. Typically, in LiZnBi, the crystal-field splitting can change

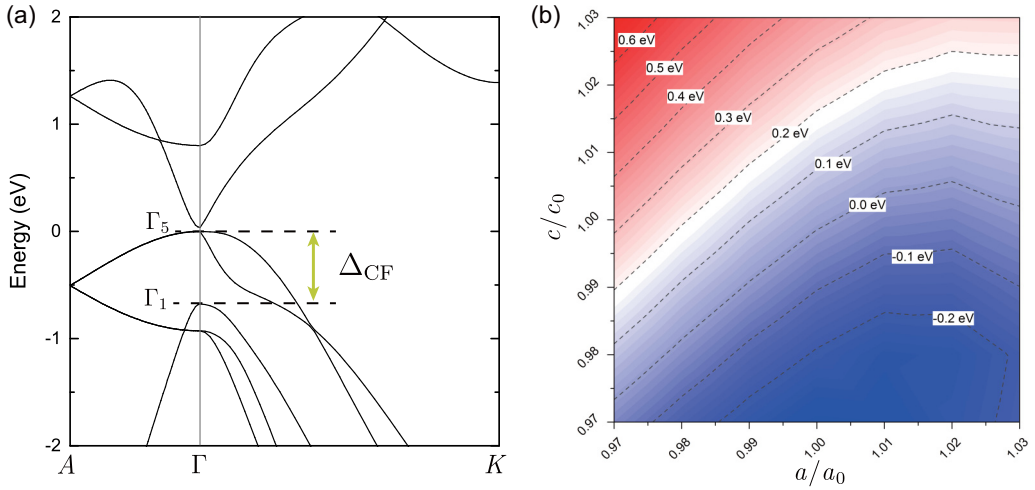

FIG. 4. (a) Band structure of the strained LiZnBi along $A-\Gamma-K$. The lattice structure is the same as that of Fig. 2(b), but the spin-orbit coupling is not included here. The valence-band maximum is set to zero. The two topmost energy levels in the valence bands are Γ_5 and Γ_1 (labeled by their representations), whose main components are $p_{x,y}$ and p_z orbitals of Bi atoms, respectively. The energy difference between these two energy levels is defined as the magnitude of crystal-field splitting, $\Delta_{\mathrm{CF}} = E[\Gamma_5] - E[\Gamma_1]$. (b) Δ_{CF} vs two lattice constants a,c with the contours (black dashed lines) labeled by the corresponding values. The inner atomic coordinates are all fully relaxed before calculating the electronic structure.

as large as several-hundred millielectron volts with ~1% strain.

When SOC is considered, the energy level Γ_5 in Fig. 4(a) splits into two doubly degenerate energy levels in which the Γ_9 state is the one closer to the Fermi level. Meanwhile, the energy level Γ_1 in Fig. 4(a) transforms to $\Gamma_7(p)$. So, for the low-energy states, we have $\Gamma_5 \Rightarrow \Gamma_9$, $\Gamma_1 \Rightarrow \Gamma_7(p)$. The gap between Γ_9 and $\Gamma_7(p)$ is affected by two factors—spin-orbit coupling and crystal-field splitting. When a small anisotropic strain is applied, the crystal-field splitting should be the key factor. And our calculations support this argument. The contour plot of $E[\Gamma_9] - E[\Gamma_7(p)]$ versus the two lattice constants a,c is shown in Fig. 5(a). One can see that the gap between Γ_9 and $\Gamma_7(p)$ indeed shares the same pattern with the crystal-field splitting Δ_{CF} shown in Fig. 4(b). As $\frac{c}{a}$ increases, the gap or splitting becomes larger and correspondingly the color becomes more red in both contour plots. Now, we are ready to explain how the strain changes the low-energy band structure in Fig. 2(b), especially the band order at the Γ point that is important for understanding the appearance of the Dirac fermion in the present system. In the unstrained case, the band order at the Γ point is $\Gamma_7(p) > \Gamma_9 > \Gamma_8 > \Gamma_7(s)$, as shown in Fig. 2(a). When we apply the strain to decrease a or enlarge c, the crystal-field splitting will reverse the band order between Γ_9 and $\Gamma_7(p)$, as discussed above. Figure 5(b) shows the contour plot of $E[\Gamma_8] - E[\Gamma_7(p)]$. In general, the decrease of a and increase of c tend to align the Zn-Bi bonds with the c axis and push up the antibonding state of the Bi-p_z orbital and Zn-s orbital (Γ_8 state). For the strained case [see Fig. 2(b)], our calculations indicate that the strain actually makes Γ_8

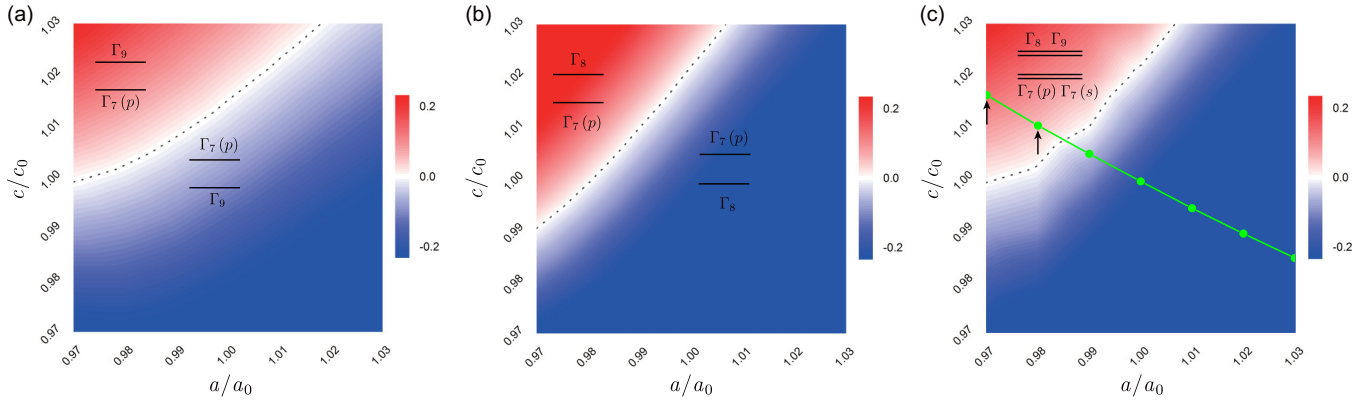

FIG. 5. Energy differences between low-energy levels at the Γ point in LiZnBi with different lattice constants. (a) $E[\Gamma_9] - E[\Gamma_7(p)]$, (b) $E[\Gamma_8] - E[\Gamma_7(p)]$, and (c) $\min\{E[\Gamma_8], E[\Gamma_9]\} - \max\{E[\Gamma_7(p)], E[\Gamma_7(s)]\}$. The black dotted lines denote the zero-energy difference. The green line in (c) represents the effect of the biaxial strain in the basal plane. For each green dot, c is determined by searching for the lowest-energy structure with a fixed. And it is found that LiZnBi is an ideal Dirac semimetal when $a = 0.97a_0$ or $0.98a_0$ (pointed out by black arrows). The atomic coordinates are fully relaxed before electronic structure calculations.

be the topmost energy level and we have the band order of $\Gamma_8 > \Gamma_9 > \Gamma_7(p)$. Moreover, a small anisotropic strain has little influence on the s orbital if the unit-cell volume barely changes. Therefore, the $\Gamma_7(s)$ state still has the lowest-energy level and there exists one band inversion between Γ_9 and $\Gamma_7(s)$ at the Γ point. Away from the Γ point, we have a finite global gap at the $k_z = 0$ plane and two band crossings between $\Gamma_7(p)$ and Γ_9 along the A-Γ-A line.

For the strained LiZnBi, the global band gap at the $k_z = 0$ plane [as shown in Fig. 2(b)] is critical for observing the topological properties of Dirac semimetals because the crossing points are separated from other states in the momentum space under this situation. We find that if $\min\{E[\Gamma_8], E[\Gamma_9]\}$ is higher than $\max\{E[\Gamma_7(p)], E[\Gamma_7(s)]\}$, this kind of global band gap can be observed generally. To simplify the study of other strain conditions, we can approximately use the positive band gap at the Γ point between $\min\{E[\Gamma_8], E[\Gamma_9]\}$ and $\max\{E[\Gamma_7(p)], E[\Gamma_7(s)]\}$ as the signature of realizing the same band structure as that in Fig. 2(b). The variation of that positive band gap with different lattice constants is shown in Fig. 5(c): in general, smaller a and larger c favor the positive band gap, consistent with our previous argument. Furthermore, we propose that about 2% biaxial in-plane compressive strain can reveal the topological properties of the Dirac nodes in LiZnBi [the green line in Fig. 5(c)], which could be realized in experiments by growing LiZnBi on a substrate with smaller in-plane lattice constant.

IV. CONCLUSIONS

In summary, our first-principles calculations indicate that LiZnBi, one of the hexagonal ABC compounds, is a 3D Dirac semimetal, but its topological nodes bury inside hole pockets of bulk states. When an in-plane compressive strain and/or out-of-plane tensile strain is applied, new emergent Dirac nodes are separated from the bulk states in the momentum space and LiZnBi becomes an ideal Dirac semimetal. This finding is confirmed by our surface state calculations in which Fermi arcs are observed to connect two projected Dirac points on the (100) surface. Furthermore, we demonstrate the physical mechanism for the strain effect on low-energy band structures in LiZnBi and find that a small strain facilitates the experimental observation of its topological Fermi arcs. Therefore, via growing on proper substrates (such as LiZnSb [37]), the nontrivial topological properties in LiZnBi are achievable in experiments. Our results not only unveil a candidate of Dirac semimetal with great versatility, but also provide a promising platform for further investigations of mutual effects between ferroelectricity and nontrivial topology.

ACKNOWLEDGMENTS

Y.X. acknowledges support from Tsinghua University Initiative Scientific Research Program and the National Thousand-Young-Talents Program. This work was supported by the Ministry of Science and Technology of China (Grant No. 2016YFA0301001) and the National Natural Science Foundation of China (Grants No. 11674188 and No. 11334006).

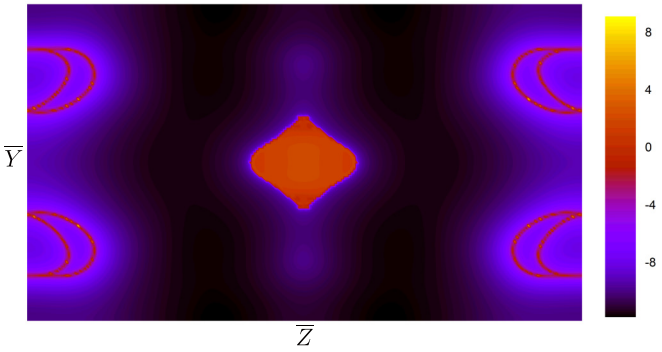

FIG. 6. The constant-energy contour at E_D^0 on the (100) surface of LiZnBi in the unstrained case. E_D^0 is the energy level of the 3D Dirac node and the corresponding bulk band structure is shown in Fig. 2(a).

APPENDIX A: (100) SURFACE STATES IN THE UNSTRAINED LiZnBi

In the surface states on the (100) surface, the 3D Dirac nodes are projected onto two distinct points. But the projections are invisible in the constant-energy contour in Fig. 6 as they merge into the normal surface states.

APPENDIX B: $\mathbb{Z}_2$ INDEX OF LiZnBi IN THE STRAINED STRUCTURE

Besides the band inversion shown in Fig. 2(b), the evaluation of the $\mathbb{Z}_2$ index can directly identify the nontrivial topology in the strained LiZnBi. Because the inversion symmetry is absent, the $\mathbb{Z}_2$ index at the Γ-M-K plane is determined by calculating the Wannier charge centers (WCCs). The results are shown in Fig. 7. The center of the largest gap jumps over seven WCC bands from Γ to M. The number of the total jumps is odd, confirming the nonzero $\mathbb{Z}_2$ index in the strained LiZnBi.

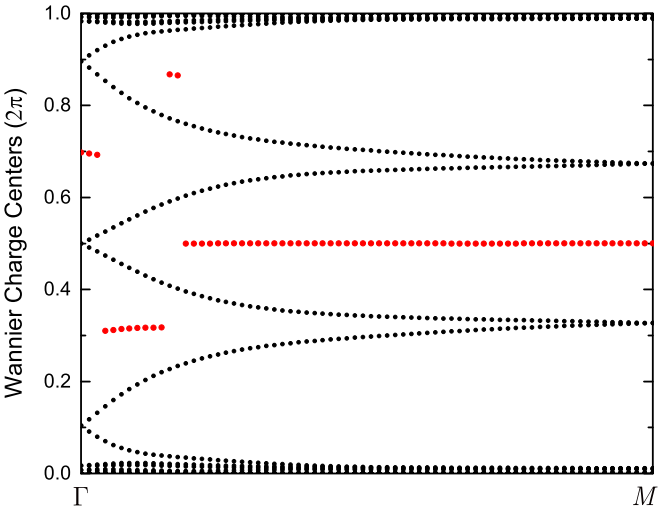

FIG. 7. WCCs along the Γ-M at the Γ-M-K plane are presented by black dots. The red dots correspond to the center of the largest WCC gap at the k point between Γ and M.

APPENDIX C: EFFECTIVE HAMILTONIAN

As stated in the main text, it is the band inversion between Γ_9 and $\Gamma_7(s)$ at the Γ point [shown in Fig. 2(b)] that induces the nontrivial topology. But at the Γ point, the $\Gamma_7(p)$ is above $\Gamma_7(s)$ and the coupling between these two bands along $A-\Gamma$ strongly pushes down s-orbital dominate states near the Γ point. Because Γ_9 and $\Gamma_7(p)$ are much closer to the Fermi level than $\Gamma_7(s)$ and the low-energy Dirac point is the crossing between bands belonging to Γ_9 and Γ_7 representations, we can exploit a minimal basis set $|\Gamma_9,\frac{3}{2}\rangle$, $|\Gamma_9,-\frac{3}{2}\rangle$, $|\Gamma_7(p),\frac{1}{2}\rangle$, $|\Gamma_7(p),-\frac{1}{2}\rangle$ to construct an effective Hamiltonian around the Γ point by following the crystal symmetry and time-reversal symmetry. Then we have

$$\mathcal{H}(\vec{k})=\epsilon_0(\vec{k})+\begin{pmatrix} M(\vec{k}) & 0 & Ak_- & 0 \\ 0 & M(\vec{k}) & 0 & -Ak_+ \\ Ak_+ & 0 & -M(\vec{k}) & Dk_- \\ 0 & -Ak_- & Dk_+ & -M(\vec{k}) \end{pmatrix}, \tag{C1}$$

where $k_\pm=k_x\pm ik_y$, $\epsilon_0(\vec{k})=C_0+C_1k_z^2+C_2(k_x^2+k_y^2)$, and $M(\vec{k})=M_0+M_1k_z^2+M_2(k_x^2+k_y^2)$. The nonvanishing terms $Dk_\pm$ result from the intrinsic inversion symmetry breaking. Fitting the first-principles calculations gives $C_0=0.203$ eV, $C_1=25.465$ eV/Å^2, $C_2=3.184$ eV/Å^2, $M_0=0.118$ eV, $M_1=-30.017$ eV/Å^2, $M_2=-8.396$ eV/Å^2, $A=4.570$ eV/Å, and $D=3.582$ eV/Å. Based on the fitting results, we can deduce the Dirac point by setting $M(k_x=0,k_y=0,k_z)=0$. The result is $0.076\times 2\pi/c$, very close to $k_z^D=0.074\times 2\pi/c$ in Fig. 2(b). Due to the inversion asymmetry, the in-plane velocity around the Dirac point takes two values, $\sqrt{A^2+D^2/4}\pm D/2$ (3.12 eV/Å and 6.70 eV/Å).

[1] H. Weng, X. Dai, and Z. Fang, J. Phys.: Condens. Matter **28**, 303001 (2016).
[2] X. Wan, A. M. Turner, A. Vishwanath, and S. Y. Savrasov, Phys. Rev. B **83**, 205101 (2011).
[3] L. Balents, Physics **4**, 36 (2011).
[4] Z. Wang, Y. Sun, X.-Q. Chen, C. Franchini, G. Xu, H. Weng, X. Dai, and Z. Fang, Phys. Rev. B **85**, 195320 (2012).
[5] S.-Y. Xu, C. Liu, S. K. Kushwaha, R. Sankar, J. W. Krizan, I. Belopolski, M. Neupane, G. Bian, N. Alidoust, T.-R. Chang, H.-T. Jeng, C.-Y. Huang, W.-F. Tsai, H. Lin, P. P. Shibayev, F.-C. Chou, R. J. Cava, and M. Z. Hasan, Science **347**, 294 (2015).
[6] I. Yu. Sklyadneva, I. P. Rusinov, R. Heid, K.-P. Bohnen, P. M. Echenique, H. Weng, and E. V. Chulkov, Sci. Rep. **6**, 24137 (2016).
[7] S. A. Parameswaran, T. Grover, D. A. Abanin, D. A. Pesin, and A. Vishwanath, Phys. Rev. X **4**, 031035 (2014).
[8] T. Liang, Q. Gibson, M. N. Ali, M. Liu, R. J. Cava, and N. P. Ong, Nat. Mater. **14**, 280 (2015).
[9] Y. Baum, E. Berg, S. A. Parameswaran, and A. Stern, Phys. Rev. X **5**, 041046 (2015).
[10] J. Xiong, S. K. Kushwaha, T. Liang, J. W. Krizan, M. Hirschberger, W. Wang, R. J. Cava, and N. P. Ong, Science **350**, 413 (2015).
[11] H. Weng, C. Fang, Z. Fang, B. A. Bernevig, and X. Dai, Phys. Rev. X **5**, 011029 (2015).
[12] S.-M. Huang, S.-Y. Xu, I. Belopolski, C.-C. Lee, G. Chang, B. Wang, N. Alidoust, G. Bian, M. Neupane, C. Zhang, S. Jia, A. Bansil, H. Lin, and M. Z. Hasan, Nat. Commun. **6**, 7373 (2015).
[13] Z. K. Liu, B. Zhou, Y. Zhang, Z. J. Wang, H. M. Weng, D. Prabhakaran, S.-K. Mo, Z. X. Shen, Z. Fang, X. Dai, Z. Hussain, and Y. L. Chen, Science **343**, 864 (2014).
[14] Z. Wang, H. Weng, Q. Wu, X. Dai, and Z. Fang, Phys. Rev. B **88**, 125427 (2013).
[15] Z. K. Liu, J. Jiang, B. Zhou, Z. J. Wang, Y. Zhang, H. M. Weng, D. Prabhakaran, S.-K. Mo, H. Peng, P. Dudin, T. Kim, M. Hoesch, Z. Fang, X. Dai, Z. X. Shen, D. L. Feng, Z. Hussain, and Y. L. Chen, Nat. Mater. **13**, 677 (2014).
[16] S. M. Young, S. Zaheer, J. C. Y. Teo, C. L. Kane, E. J. Mele, and A. M. Rappe, Phys. Rev. Lett. **108**, 140405 (2012).
[17] P. Tang, Q. Zhou, G. Xu, and S.-C. Zhang, Nat. Phys. **12**, 1100 (2016).
[18] A. A. Soluyanov, D. Gresch, Z. Wang, Q. Wu, M. Troyer, X. Dai, and B. A. Bernevig, Nature (London) **527**, 495 (2015).
[19] H. Huang, S. Zhou, and W. Duan, Phys. Rev. B **94**, 121117 (2016).
[20] M. Yan, H. Huang, K. Zhang, E. Wang, W. Yao, K. Deng, G. Wan, H. Zhang, M. Arita, H. Yang, Z. Sun, H. Yao, Y. Wu, S. Fan, W. Duan, and S. Zhou, Nat. Commun. **8**, 257 (2017).
[21] K. Zhang, M. Yan, H. Zhang, H. Huang, M. Arita, Z. Sun, W. Duan, Y. Wu, and S. Zhou, Phys. Rev. B **96**, 125102 (2017).
[22] F. Y. Bruno, A. Tamai, Q. S. Wu, I. Cucchi, C. Barreteau, A. de la Torre, S. McKeown Walker, S. Riccò, Z. Wang, T. K. Kim, M. Hoesch, M. Shi, N. C. Plumb, E. Giannini, A. A. Soluyanov, and F. Baumberger, Phys. Rev. B **94**, 121112(R) (2016).
[23] K. Deng, G. Wan, P. Deng, K. Zhang, S. Ding, E. Wang, M. Yan, H. Huang, H. Zhang, Z. Xu, J. Denlinger, A. Fedorov, H. Yang, W. Duan, H. Yao, Y. Wu, S. Fan, H. Zhang, X. Chen, and S. Zhou, Nat. Phys. **12**, 1105 (2016).
[24] J. W. Bennett, K. F. Garrity, K. M. Rabe, and D. Vanderbilt, Phys. Rev. Lett. **109**, 167602 (2012).
[25] D. Di Sante, P. Barone, A. Stroppa, K. F. Garrity, D. Vanderbilt, and S. Picozzi, Phys. Rev. Lett. **117**, 076401 (2016).
[26] S. Liu, Y. Kim, L. Z. Tan, and A. M. Rappe, Nano Lett. **16**, 1663 (2016).
[27] P. E. Blöchl, Phys. Rev. B **50**, 17953 (1994).
[28] G. Kresse and D. Joubert, Phys. Rev. B **59**, 1758 (1999).
[29] G. Kresse and J. Furthmüller, Phys. Rev. B **54**, 11169 (1996).
[30] D. M. Ceperley and B. J. Alder, Phys. Rev. Lett. **45**, 566 (1980).
[31] J. P. Perdew and A. Zunger, Phys. Rev. B **23**, 5048 (1981).
[32] F. Tran and P. Blaha, Phys. Rev. Lett. **102**, 226401 (2009).
[33] A. D. Becke and E. R. Johnson, J. Chem. Phys. **124**, 221101 (2006).
[34] A. A. Mostofi, J. R. Yates, Y.-S. Lee, I. Souza, D. Vanderbilt, and N. Marzari, Comput. Phys. Commun. **178**, 685 (2008).

[35] M. P. L. Sancho, J. M. L. Sancho, J. M. L. Sancho, and J. Rubio, J. Phys. F **15**, 851 (1985).
[36] F. Casper, R. Seshadri, and C. Felser, Phys. Status Solidi A **206**, 1090 (2009).
[37] A. Belsky, M. Hellenbrandt, V. L. Karen, and P. Luksch, Acta Crystallogr. Sect. B **58**, 364 (2002).
[38] G. K. H. Madsen, J. Am. Chem. Soc. **128**, 12140 (2006).
[39] B.-J. Yang and N. Nagaosa, Nat. Commun. **5**, 4898 (2014).
[40] C. Fang, M. J. Gilbert, X. Dai, and B. A. Bernevig, Phys. Rev. Lett. **108**, 266802 (2012).
[41] S. S. Tsirkin, I. Souza, and D. Vanderbilt, Phys. Rev. B **96**, 045102 (2017).
[42] C. L. Kane and E. J. Mele, Phys. Rev. Lett. **95**, 146802 (2005).
[43] A. A. Soluyanov and D. Vanderbilt, Phys. Rev. B **83**, 235401 (2011).
[44] Y. M. Sirenko, J. B. Jeon, B. C. Lee, K. W. Kim, M. A. Littlejohn, M. A. Stroscio, and G. J. Iafrate, Phys. Rev. B **55**, 4360 (1997).